On the Feasibility of Breast Cancer Imaging Systems at Millimeter-Waves Frequencies

Simona Di Meo, *Student Member, IEEE*, Pedro Fidel Espín-López, *Student Member, IEEE*, Andrea Martellosio, *Student Member, IEEE*, Marco Pasian, *Senior Member, IEEE*, Giulia Matrone, *Member, IEEE*, Maurizio Bozzi, *Senior Member, IEEE*, Giovanni Magenes, *Member, IEEE*, Andrea Mazzanti, *Senior Member, IEEE*, Luca Perregrini, *Fellow, IEEE*, Francesco Svelto, *Fellow, IEEE*, Paul Eugene Summers, Giuseppe Renne, Lorenzo Preda, and Massimo Bellomi
(Invited Paper)

***Abstract*— Medical imaging currently relies on several techniques, including X-rays, magnetic resonance, and echography. However, these techniques exhibit drawbacks, and alternative approaches are required. Microwave imaging has been proposed as a possible solution, especially for breast cancer imaging. However, most of these systems work with a central frequency of a few gigahertz, and this leads to a suboptimum resolution, which can jeopardize the image quality. Millimeter waves can provide superior resolutions, at the cost of a lower penetration depth within the breast tissue. In addition, a significant fraction of the power generated by a mm-wave imaging system would be reflected back from the skin. For these reasons, and also considering that mm-wave transmitters and receivers have been historically outperformed by microwave counterparts in terms of available power and sensitivity, mm-wave imaging has not been considered a possible solution. This paper contributes to demonstrate a paradigm shift toward the possible use of mm-waves for breast cancer imaging of targets a few centimeter below the skin, a useful penetration depth for several cases. All key points are addressed using analytical, full-wave, and multiphysics simulations, including the system architecture (linear and conformal), the safety aspects (power density, specific absorption rate, and temperature increase), and the use of realistic breast models derived from ex vivo measurements.**

Manuscript received October 18, 2016; revised February 3, 2017; accepted February 8, 2017. This work was supported by the Italian Association for Cancer Research.

S. Di Meo, A. Martellosio, M. Pasian, G. Matrone, M. Bozzi, G. Magenes, A. Mazzanti, L. Perregrini, and F. Svelto are with the Department of Electrical, Computer and Biomedical Engineering, University of Pavia, 27100 Pavia, Italy (e-mail: simona.dimeo01@ateneopv.it; andrea.martellosio01@ateneopv.it; marco.pasian@unipv.it; giulia.matrone@unipv.it; maurizio.bozzi@unipv.it; giovanni.magenes@unipv.it; andrea.mazzanti@unipv.it; luca.perregrini@unipv.it; francesco.svelto@unipv.it).

P. F. Espín-López is with the Department of Radiology, European Institute of Oncology, 20146 Milan, Italy, and also with the Department of Electrical, Computer and Biomedical Engineering, University of Pavia, 27100 Pavia, Italy (e-mail: pedrofi.espin@gmail.com).

P. E. Summers and M. Bellomi are with the Department of Radiology, European Institute of Oncology, 20146 Milan, Italy (e-mail: paul.summers@ieo.it; massimo.bellomi@ieo.it).

G. Renne is with the Department of Anatomy and Pathology, European Institute of Oncology, 20146 Milan, Italy (e-mail: giuseppe.renne@ieo.it).

L. Preda is with the Department of Radiology, European Institute of Oncology, 20146 Milan, Italy, also with the Department of Clinical-Surgical, Diagnostic and Pediatric Sciences, University of Pavia, 27100 Pavia, Italy, and also with the National Center of Oncological Hadrontherapy (CNAO Foundation), 27100 Pavia, Italy (e-mail: lorenzo.preda@unipv.it).

Color versions of one or more of the figures in this paper are available online at http://ieeexplore.ieee.org.

Digital Object Identifier 10.1109/TMTT.2017.2672938

***Index Terms*— Antenna array, breast cancer, conformal array, dielectric characterization, dielectric properties, *ex vivo* tissues, microwave imaging, mm-wave imaging, multiphysics, power density, specific absorption rate (SAR).**

I. Introduction

BREAST cancer is a leading disease worldwide affecting a significant fraction of women. Breast cancer detection is currently achieved (along with manual palpation) by using three different imaging techniques, i.e., X-ray mammography, ultrasound echography, and magnetic resonance. However, all techniques have some disadvantages. Echography is strongly dependent on the physician's ability, thus generating an extremely variable success rate; X-ray mammography is based on uncomfortable compression and ionizing radiation, thus preventing its use for mass periodical screening; magnetic resonance requires an extremely large and costly machine, thus preventing its use for mass periodical screening. Therefore, alternative and/or complementary imaging techniques are welcomed.

Microwave imaging is proposed as a possible solution to this problem [1]–[6]. The most important advantages are the use of nonionizing radiation and the availability of relatively low-cost equipment. In addition, all proposed systems require no (or smooth) compression and are conceived to be operator independent. Different system architectures have been exploited, the most common being tomography and multistatic radar, and they all rely on the contrast between the dielectric proprieties of normal and tumorous breast tissues [7], [8].

All proposed microwave-imaging systems to date share similar operational frequencies, not exceeding a few gigahertz. Consequently, they tend to lack in resolution, a critical problem for breast imaging, because a low resolution is directly translated into a difficult morphological reference for the physician [1], [9]. The natural solution to this problem relies on the use of higher frequencies, which allows for a better spatial resolution and a downscaling of many components (in particular sensors and antennas). However, the main problem attributed to the use of higher frequencies, in particular mm-waves, is the low penetration depth. For this reason, in the framework of an increasing interest for the use of higher frequencies in the field of biomedical applications [10],

systems working at mm-waves and beyond (THz-regime) have been often limited to applications where the penetration depth is not a key parameter, such as skin cancer detection, cancer margins detection during surgical removal, corneal, and dental monitoring [11]–[14].

However, it has been recently suggested that this limitation can be overcome to provide breast imaging at different frequencies, up to the THz and infrared spectrum [15]–[19]. In particular, mm-wave frequencies deserve high interest, because they represent a natural continuation of a well-established research path at microwave frequencies, and because the latest technological developments in the field of automotive (car radar), security (body scanner), and communication (short-range links) markets can now provide suitable transmitters and receivers at a relatively moderate cost [20]–[22].

This paper discusses the possibility of using mm-waves at around 30 GHz for breast cancer imaging, taking into account for the first time newly available experimental values for the dielectric properties of breast tissues up to 50 GHz [23], [24]. In addition, also the safety aspects related to the body exposure to relatively high levels of electromagnetic power are considered [25], [26]. It has been demonstrated that, in several cases, a penetration depth of a few centimeters is possible, while maintaining reasonable safety margins, and specifically in terms of temperature increase. In addition, design guidelines are provided for future system architectures. This paper is organized as follows. Section II discusses the safety limits imposed by current regulations and, using full-wave and multiphysics models, it calculates the power density, the specific absorption rate (SAR), and the temperature increase within the body for different power levels. Sections III and IV discuss on the basis of analytical equations the system architecture, in particular, in terms of number and position of the radiators, providing design guidelines for two different array configuration, i.e., linear and conformal. Section V demonstrates two examples of image formation within a relevant simulated breast.

II. Safety Limits

The safety aspects related to the exposure to nonionizing electromagnetic fields are discussed by a number of scientific panels, including the independent International Commission on NonIonizing Radiation Protection (ICNIRP), which is considered by many regulatory bodies, including the European Union, in establishing safety recommendations [27]. Notably, the ICNIRP data are divided into two parts: the first part, referred to as *basic restrictions*, concerns quantities directly related to the biological effects within the body, e.g., the SAR, and an extract is summarized in Table I. The second part, referred to as *reference levels*, concerns quantities, mathematically derived or extrapolated from the quantities reported in Table I, but easier to measure or simulate, such as the electric or magnetic field, and an extract is summarized in Table II. The mandatory limits are those summarized in Table I (*basic restrictions*), and because of the extrapolations necessary to move from Tables I to II, *reference levels* are calculated with a safe margin in such a way that compliance with *reference levels* (easier to be verified) automatically leads to compliance with *basic restrictions* (directly related to health effects). Conversely, if *reference levels* are exceeded, this does not automatically mean that the *basic restrictions* are not met, and more accurate analyses and verifications are required.

TABLE I
ICNIRP Basic Restrictions for General Public (Values in Parenthesis Are Occupational Limits)

Frequency	Current density (mA/m^2) r.m.s.	Localized SAR (head and trunk) (W/kg)	Power density (W/m^2)
1–100 kHz	$f_{[Hz]}$ / 500	not applicable	not applicable
0.1–10 MHz	$f_{[Hz]}$ / 500	0.08 (0.4)	not applicable
0.01–10 GHz	not applicable	0.08 (0.4)	not applicable
10–300 GHz	not applicable	not applicable	10 (50)

TABLE II
ICNIRP Reference Levels for General Public (Values in Parenthesis Are Occupational Limits)

Frequency	$\lvert\mathbf{E}\rvert$ (V/m) r.m.s.	$\lvert\mathbf{H}\rvert$ (A/m) r.m.s.	Power density (W/m^2)
0.8–3 kHz	250 / $f_{[kHz]}$	5	not applicable
3–150 kHz	87	5	not applicable
0.15–1 MHz	87	0.73 / $f_{[MHz]}$	not applicable
1–10 MHz	87 / $f_{[MHz]}^{1/2}$	0.73 / $f_{[MHz]}$	not applicable
10–400 MHz	28	0.073	2
400–2000 MHz	1.375 · $f_{[MHz]}^{1/2}$	0.0037 · $f_{[MHz]}^{1/2}$	$f_{[MHz]}$ / 200
2–300 GHz	61 (137)	0.16 (0.36)	10 (50)

However, the values reported in Tables I and II are affected by a number of limitations when applied to mm-wave frequencies. First, these limits were derived before the rapid growth in the availability of mm-wave devices. Second, above 10 GHz, a limit in terms of power density is given (10 and 50 W/m^2 for general and occupational public, respectively), but recent studies pointed out that current exposure guidelines may be not fully appropriate [25]. This is because the evaluation of the power density in a complicated scenario, as it can often be the case for biological applications where the radiators may be in proximity (i.e., near-field) of highly reflective tissues (e.g., skin), is often not univocal. Conversely, the results may vary depending on the methods used for the numerical or experimental investigation.

On the other hand, the SAR, probably the common parameter to evaluate the interaction between the electromagnetic fields and the biological target, is not given at mm-wave frequencies. This reflects recent studies where a possible uncorrelation between the SAR and the temperature increase in the tissue at mm-wave frequencies is demonstrated [25]. A number of studies have tried to address these problems, providing a more detailed analysis of the interaction of human tissues with mm-waves [28].

However, for many applications, e.g., communication devices, the radiators are not intended to directly illuminate

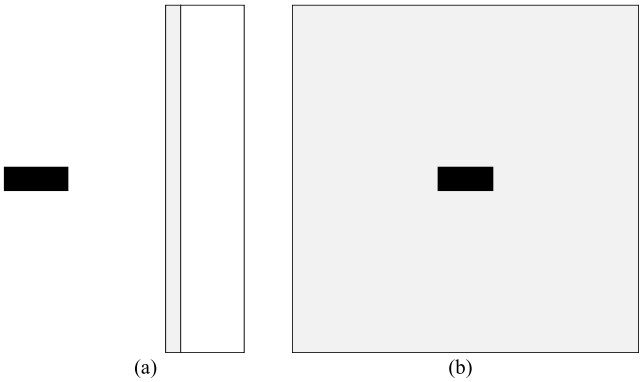

Fig. 1. Schema of the full-wave/multiphysics model used to calculate the safety limits. The WR28 open-ended waveguide is depicted in black, the skin in light gray, and the breast tissue in white. (a) Side view. (b) Front view.

human tissues, and the presence of electromagnetic fields within the body is, ideally, something to be minimized, as traditionally pursued for mobile devices at both microwave and mm-wave frequencies [29]. Two recent applications, that involve directly illuminating the human body, are mm-wave body scanners and microwave breast imaging systems. However, mm-wave body scanners are not intended to penetrate below the skin, and a very low power density (around 6 mW/m^2) is supposed to be generated [30]. On the contrary, microwave breast imaging systems seek to penetrate the whole breast. While supporting the safety of these systems, previous studies have confirmed that the highest temperature increase is identified within the skin, and this risk increases with frequency [31]–[33].

It is, therefore, clear that for an mm-wave breast cancer imaging system, designed to deliberately illuminate human breasts in such a way that a penetration depth of a few cm can be achieved, it is vital to properly evaluate the interaction of mm-waves with breast tissues, in particular, the skin. In order to provide a complete overview of the most relevant dosimetric quantities at play, a full-wave model (based on a commercial software employing a time-domain method with multiphysics capabilities) is developed to calculate the power density, the SAR, and the temperature increase within the breast tissue. In particular, the full-wave approach allows possible limitations based on far-field formulation to be overcome, while the multiphysics approach, which includes bio-heat equations to calculate the thermal power dissipated because of the blood circulation, allows to calculate the temperature increase, which is particularly relevant given the current debate on regulations in mm-waves.

The breast model, shown in Fig. 1, consists of two planar layers. The dielectric properties of the outer layer are tailored to mimic the normal human skin, while those of the inner layer are tailored to mimic normal human breast tissues with a high adipose content [23], [34]. As an example, it is worth noting that, according to an experimental campaign where the *ex vivo* dielectric permittivity of breast tissues was measured on more than 200 samples obtained from more than 50 patients, breast samples with an adipose content greater than 80% account for a large fraction (almost one out of two) of all the measured samples. The thicknesses of the tissues are 2 and 8 mm for the skin and the breast tissue, respectively. In particular, the thickness of the skin is designed to be representative of normal biological conditions, while the thickness of the breast tissue is designed to be thick enough to avoid significant reflections at the back-end of the layer itself. All details are summarized in Table III, which also includes the properties of the tumorous tissue, used in the calculations presented in Sections IV and V. Furthermore, as the free-space wavelength at 30 GHz is around 10 mm, well below the radius of curvature of breasts, the planar multilayer model is a viable choice. The lateral dimension of the planar multilayer model shown in Fig. 1 is intentionally designed to be 44.72 mm to comply with ICNIRP guidelines. Indeed, the thresholds reported in Tables I and II are averaged for a total area exposed to the electromagnetic radiation of 20 cm^2.

TABLE III
PARAMETERS OF THE BREAST MODEL AT 30 GHZ

Parameter	Skin [34]	Breast tissue [23]	Tumorous tissue [24]
e'	15.51	3	19.02
e''	16.23	0.3	20.03
thickness [mm]	2	8	n.a.

For the full-wave model, a continuous wave exposure is assumed, and for the calculation of the thermal effects (multiphysics simulation), an exposure time T_e (i.e., the time required to reach a steady state from the thermal point of view) of around 115 s is accounted for, again according to the ICNIRP guidelines. In particular, these guidelines indicate an exposure time calculated as $T_e = 68/f^{1.05}$ (where f is the working frequency measured in GHz, and T_e is measured in minutes). The breast model is illuminated using as the antenna an open-ended rectangular waveguide WR28 (7.112 mm $\times$ 3.556 mm). For completeness, the antenna can be placed at a variable distance from the skin. Fig. 2 shows the simulated results for the power density, calculated at the skin surface, i.e., at the maximum. In particular, as an example, Fig. 2(a) shows the power density for different distances between the antenna and the skin surface, using a transmitting power $P_{\text{tx}} = 100$ mW. It is observed that the near-field nature of the problem yields a dependence on the distance different from the usual square law typical of the far-field propagation. For example, at around 20 mm, the power density is around 8 W/m^2, while at around 40 mm the power density is around 6 W/m^2. On the other hand, Fig. 2(b) shows, as an example, the power density for different values of the transmitting power P_{tx}, using an antenna-to-skin distance of around 15 mm. As expected, it is observed that the trend is described in linear proportion. For example, at 0.1 W, the power density is around 10 W/m^2, while at 1 W, the power density is around 100 W/m^2. Overall, it is shown that it is possible to use both parameters, i.e., transmitting power and antenna-to-skin distance, to meet either the general public (10 W/m^2) or the occupational limits (50 W/m^2), reported in Tables I and II.

Although the SAR limits are not relevant for mm-wave frequencies, and as described earlier, no thresholds are given, as already discussed, Fig. 3 shows the SAR calculated for an

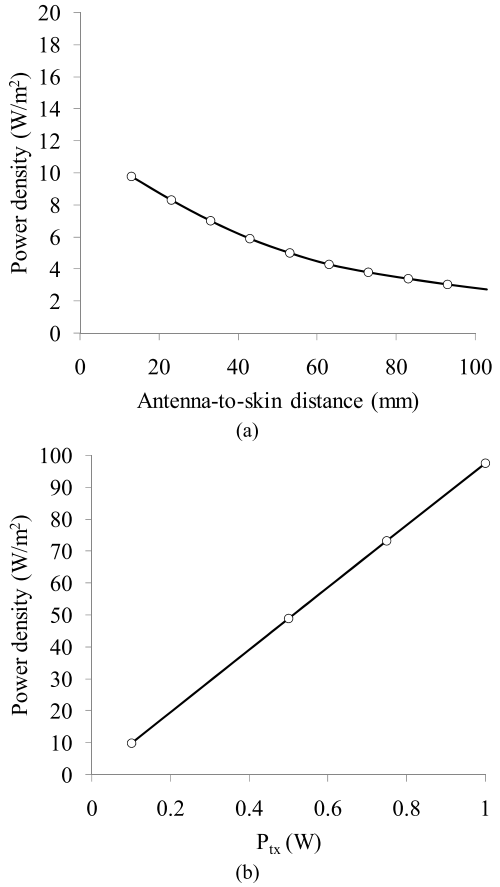

Fig. 2. Power density at the skin surface for (a) different distances between the antenna and the skin surface, using a transmitting power $P_{\text{tx}} = 100$ mW and (b) different values of the transmitting power P_{tx}, using an antenna-to-skin distance of around 15 mm.

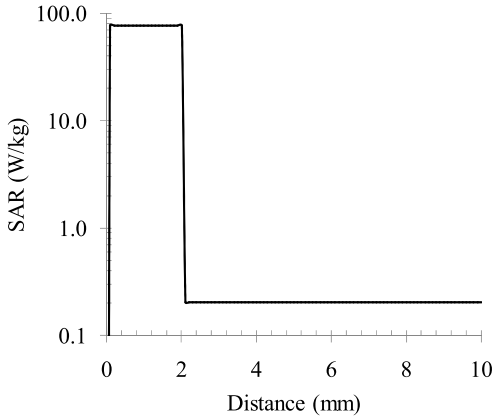

Fig. 3. Power density within the breast model shown in Fig. 1 calculated for a transmitting power $P_{\text{tx}} = 100$ mW and an antenna-to-skin distance of around 15 mm.

antenna-to-skin distance of around 15 mm, and a transmitting power $P_{\text{tx}} = 100$ mW. It is observed that the highest values for the SAR occur in the skin, while the amount of power in the breast tissue is not expected to create relevant effects for the safety aspects.

As anticipated, a multiphysics approach, including bioheat equations to calculate the thermal power dissipated because of the blood circulation, is required to provide the most important parameter, which is the temperature increase. Indeed, since

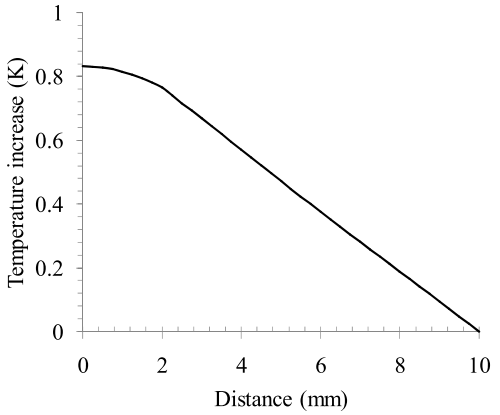

Fig. 4. Temperature increase within the breast model shown in Fig. 1 calculated for a transmitting power $P_{\text{tx}} = 100$ mW and an antenna-to-skin distance of around 15 mm.

the most relevant biological effects on the mm-waves are expected to be associated with thermal effects, beyond the limits provided by the ICNIRP guidelines, the temperature increase represents a fundamental verification.

Fig. 4 shows the temperature increase calculated for an antenna-to-skin distance of around 15 mm, and a transmitting power $P_{\text{tx}} = 100$ mW. It is observed that the highest temperature occurs in the skin, but it remains below 1°, which can be considered a conservative limit for thermal effects [35]. In addition, it is demonstrated that the model dimension (10 mm) is enough to take into account the portion of the breast where quantities related to the safety aspects are expected to be calculated. Taking into account all these results, in particular those related to the temperature increase, a transmitting power $P_{\text{tx}} = 100$ mW is taken as the reference value for the subsequent system architecture optimization, presented in Section IV.

III. System Architecture—Overview

The working principle of the system conceived for breast cancer imaging at mm-wave frequencies, shown in Fig. 5, is based on a multistatic radar architecture. It consists of M antennas able to either transmit or receive a signal at mm-waves. In particular, while an antenna is used to transmit the signal, all the remaining $M - 1$ antennas are used to receive the backscattered signal. This procedure is repeated M times, each time using a different transmitting antenna. It is immediately calculated that the number of transmitter–receiver combinations is $M(M-1)$. Therefore, the backscattered signal (without losing generality, the target is supposed to backscatter uniformly in all directions) is collected and coherently summed $M(M-1)$ times. This improves the received power by a factor equal to $(M(M-1))^2$. At the same time, the receiver noise, supposed to be incoherent, is integrated $M(M-1)$ times. Therefore, the final signal-to-noise ratio (S/N) is improved by an improving factor $F = M(M-1)$, greatly enhancing the dynamic range of the system. However, this holds only when all received signals are equal to each other. In fact, while the noise is always integrated $M(M-1)$ times, the power received is a function of the actual collected signals.

In particular, for a generic imaging system, a source of imbalance among the received signals is the different propa-

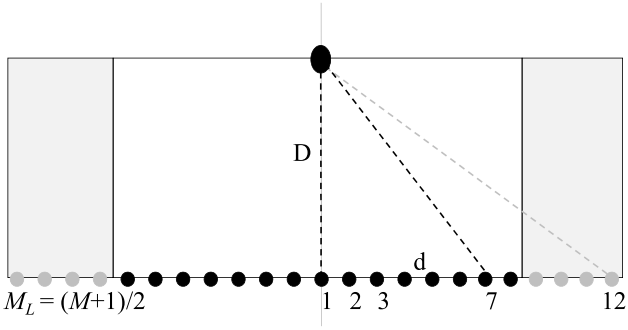

Fig. 5. Schema of the working principle. The target (black ellipse) is at a distance D from the antennas, which comprises M antennas separated by a distance d. The antennas positively contributing to the final S/N are shown as black circles, and an example of propagation path is shown from antennas #1 to #7. The antennas negatively contributing to the final S/N are shown as gray circles, and an example of propagation path is shown from antennas #1 to #12. The symmetry plane is depicted as the central light gray line. In this example $M = 23 (M_L = 1)$, while the total number of useful radiators (black circles) is 15.

gation distance. If an ideal case, with no losses is considered, the received signals will be equal to each other, thus delivering the ideal improving factor $F = M(M - 1)$, regardless of the different propagation distances. However, for real propagation media, this rigorous condition does not hold, and the ideal improving factor can only be approached when the attenuations of the different transmitter–receiver paths are similar to each other. This can be achieved when the propagation distances are similar and/or in case of a low-loss medium. As an example, imaging systems at microwave frequencies working according to this approach have been proposed [2]. Conversely, at mm-wave frequencies, the attenuation in the propagation medium may be notable, causing significantly different propagation losses even among adjacent radiators, thus partially spoiling the improving factor.

To better explain this aspect, let us consider a typical example where a hypothetical target is at a distance of $D = 5$ cm from the antenna plane, which comprises, for simplicity, only three antennas separated by a relative distance of $d = 5$ mm. In particular, antenna #1 is directly in line with the target, antenna #2 with a lateral displacement of 5 mm, and antenna #3 with a lateral displacement of 10 mm. According to the multistatic radar principle explained previously, the signal backscattered by the target is collected six times as reported in Table IV. However, each path exhibits a different propagation distance, calculated according to a ray-optics approach and reported in Table IV, slightly greater than the two-way propagation distance between the target and the antenna plane. Consequently, apart from the ideal case, where no attenuation holds and a perfect improving factor is retrieved (i.e., $F = 6$), a real propagation medium provides different relative attenuations (with respect to the shortest path), causing a reduction of the improving factor.

In the case of healthy breast tissue as the propagation medium, the attenuations are calculated by taking into account the dielectric properties at 30 GHz, already reported in Table III. The relative attenuations between different paths, shown in Table V, are as high as almost 0.5 dB, causing a not negligible reduction of the improving factor with respect to the ideal case ($F = 5.3$, Table VI). Moreover, although

TABLE IV

PROPAGATION SCHEMA FOR THE SYSTEM SHOWN IN FIG. 5

	Receiver Antenna #1		Receiver Antenna #2		Receiver Antenna #3	
	Path	Distance	Path	Distance	Path	Distance
Transmitter Antenna #1	n.a.		#1	10.02 cm	#2	10.10 cm
Transmitter Antenna #2	#3	10.02 cm	n.a.		#4	10.12 cm
Transmitter Antenna #3	#5	10.10 cm	#6	10.12 cm	n.a.	

TABLE V

RELATIVE ATTENUATION WITH RESPECT TO THE SHORTEST PATH (#1 AND #3 IN TABLE IV), MEASURED IN dB, FOR BREAST FAT AT 30 GHz

	Receiver Antenna #1	Receiver Antenna #2	Receiver Antenna #3
Transmitter Antenna #1	n.a.	0	0.37
Transmitter Antenna #2	0	n.a.	0.46
Transmitter Antenna #3	0.37	0.46	n.a.

TABLE VI

IMPROVING FACTOR FOR THE S/N FOR THE IDEAL CASE AND FOR BREAST FAT AT 30 GHz

	Ideal	Breast fat
Improving factor	6.0	5.3

the number of the antennas is limited to three to explain the working principle, it is worth observing that the difference with respect to the ideal case rapidly increases with the number of antennas.

This example clarifies that the usual benefits given by the use of a multistatic system architecture, which most often hold at microwave frequencies, should be carefully addressed at mm-wave frequencies. In particular, it is very important to design the proper number of radiators and their reciprocal locations in order to maximize the improving factor for a given penetration depth. Indeed, following the discussion reported earlier, it is expected that the system S/N can be improved with respect to the S/N of the single transmitter–receiver pair by increasing the number of radiators up to a certain threshold. Then, adding other radiators, the system S/N will begin to deteriorate, as shown in Fig. 5.

IV. SYSTEM ARCHITECTURE—LAYOUT OPTIMIZATION

One of the most important advantages of an mm-wave imaging system is the potential resolution. In particular, two different resolutions can be discussed, the range resolution δ_R and the lateral resolution δ_L. Without losing generality, let us assume a 2-D scenario, where the system is intended to form an image of the plane containing the radiators. If they are arranged along a line, as shown in Fig. 5, the range resolution δ_R is the resolution achievable along the direction normal to the antennas, while the lateral resolution δ_L is resolution achievable along the direction parallel to the antennas. In particular, the range resolution δ_R can be calculated as

$$\delta_R = \upsilon/(2B) \tag{1}$$

where υ is wave speed into the medium, and B is the signal bandwidth. Taking into account the dielectric permittivity

reported in Table III, and considering as a practical case the use of standard open-ended waveguides WR28, with a fundamental-mode bandwidth from 26.5 to 40 GHz, a range resolution $\delta_R = 6$ mm at 30 GHz can be calculated. On the other hand side, the lateral resolution δ_L is also a function of the wave speed v, but it also includes the dimension of the aperture plane, and it can be calculated as

$$\delta_L = vD/(fL) \tag{2}$$

where D is the distance from the aperture plane to the target, f is the working frequency, and $L = (M-1)d$ is the aperture dimension. As an example, for a target at a distance of $D = 5$ cm imaged with nine antennas ($L = 4$ cm), a lateral resolution of $\delta_R = 6.75$ mm at 30 GHz can be calculated, approximately that of the range resolution. It is worth observing that the wave speed v in the medium, being lower than the speed of light (around $1.7 \cdot 10^8$ m/s instead of around $3 \cdot 10^8$ m/s), contributes to enhance both resolutions.

To reduce the burden of full-wave simulation, the system architecture is designed, implementing an analytical solution based on an approximated link budget that allows testing and optimizing several different system configurations. The propagation loss for each transmitter–receiver path is calculated according to the data reported in Table VII, and computing the propagation distance according to the ray-optics approach mentioned in Section III. Given the approximated nature of the calculation, a conservative margin is taken for a number of parameters [e.g., the receiver noise figure (NF)], having in mind a subsequent verification of the final configuration by means of full-wave test cases, discussed in Section V.

The transmitted power is limited by the safety aspects reported in Section II. In particular, using $P_{\text{tx}} = 20$ dBm (100 mW), it was demonstrated that the maximum temperature increase can remain below 1 °C. At the receiver side, a reasonable NF, i.e., NF = 10 dB, and an imaging time compatible with *in vivo* human breast imaging, i.e., $T_i = 30$ min, are considered. It is worth noting that the current state of the art for the NF is well below 10 dB; thus, this choice is taken to add an extra conservative margin [36]–[38]. In addition, it is also worth noting that the imaging time is derived from the medical experience of other imaging techniques, where unavoidable patient movements, such as breathing, can be largely reduced using a prone position and a dedicated breast cup. Once the imaging time T_i is known, the available integration time T_{rx} for each receiver, hence the integration bandwidth B, can be calculated according to the number of radiators M. Indeed, as explained in Section III, the signal backscattered by the target is collected M times.

Therefore, the higher the number of antennas, the shorter is the integration time (hence, the larger the integration bandwidth) for each sweep, and, consequently, the higher is the receiver noise. As an example, reported in Table VII, with $M = 8$, an integration time $T_{\text{rx}} = 225$ s is calculated. According to state-of-the-art electronics, the entire bandwidth from 26.5 to 40 GHz is scanned in the specified integration time using an intermediate-frequency bandwidth (i.e., the integration bandwidth B) of around 18 Hz. Assuming now that the system is operated at room temperature, with a thermal noise floor of around −173 dBm/Hz, this is translated into a receiver noise of around −150 dBm. Therefore, the attenuations from the transmitter to the receiver are calculated according to the actual path geometry (as discussed in Section III for the case of three antennas) and including, on top of standard propagation losses, also the dissipation losses given by the imaginary part of the propagation medium (Table III), and extra losses taking into account the skin reflections and the target reflectivity. In particular, an overall loss of 20 dB is included in the link budget for these latter contributions, which can be estimated on the basis of the dielectric properties of the different parts (skin, normal, and tumors breast tissues, reported in Table III) and assuming that the reflections from the skin can be partially compensated for by adding a matching layer, or with a dedicated antenna design aimed at radiating directly in contact with the human body, and/or filtering out this reflection using various techniques (e.g., time-domain reflectometry, geometrical rotations of the target, and so on), as already attempted for similar applications in the microwave region [1].

TABLE VII
EXAMPLE OF SYSTEM LINK BUDGET

Parameter	Symbol	Value
Transmitted power	P_{tx}	20 dBm
Imaging time	T_i	1800 s
Number of antennas	M	8
Integration time	$T_{rx} = T_i / M$	225 s
Integration bandwidth	B	18 Hz
Thermal noise floor	N_t	-173 dBm/Hz
Receiver noise figure	NF	10 dB
Receiver noise	N	-150 dBm
System S/N	S/N	30 dB

Again, it is clear that the system layout, in particular the number of antennas, is the result of a compromise between receiver noise, system S/N, and resolution.

However, the use of the approximated link budget allows to take into account these opposite trends, analyzing several different configurations in a reasonable amount of time. Moreover, to further simplify the system model, the symmetry plane shown in Fig. 5 is exploited, working on a monolateral aperture plane. In this way, it is also included a safety margin, being the target at the side of the aperture a worst case scenario, because the number of antennas positively contributing to the final S/N is reduced. Each configuration is driven by two fundamental parameters, i.e., the target distance D from the aperture plane, and the number of monolateral antennas $M_L = (M+1)/2$, separated by a relative distance of $d = 5$ mm (free-space half wavelength). For each configuration, both the improving factor and the final system S/N are calculated. Then, a configuration is discarded from the available solutions if the improving factor is less than one or if the final S/N is lower than a realistic target at the output of the correlator, i.e., 30 dB. The results are shown in Fig. 6.

As an example, three different target distances are considered, $D = 2$ cm, $D = 4$ cm, and $D = 6$ cm. A number of results can be derived. First, as anticipated in Section III,

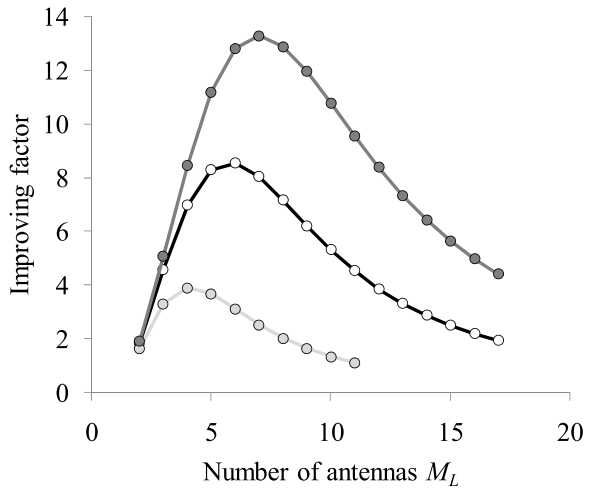

Fig. 6. Improving factor for a target distance $D = 2$ cm (light gray line), $D = 4$ cm (black line), and $D = 6$ cm (dark gray line).

in all cases, an optimum exists. For $D = 2$ cm, this optimum is represented by a number of antennas $M_L = 4$, for $D = 4$ cm, this optimum is represented by a number of antennas $M_L = 6$, while for $D = 6$ cm, this optimum is represented by a number of antennas $M_L = 7$. These are optimum for the system S/N, and for any extra antenna, the added noise would be larger than the added signal, thus reducing the system S/N. However, a possible compromise could be based on the use of a number of antennas larger than the optimum to increase the lateral resolution, at the cost of a less-than-optimum result in terms of S/N.

Second, the achieved improving factor is significantly smaller than that achievable with the ideal lossless case, and the ideal case is better approached for larger target distances, as expected. As an example, for $D = 4$ cm and $M_L = 6$ (optimum), the improving factor is around 8, around 3.75 times lower than $M_L(M_L - 1) = 30$, while for $D = 6$ cm and $M_L = 7$ (optimum), the improving factor is around 13, around 3.23 times lower than $M_L(M_L - 1) = 42$. Better approximations of the ideal case would be obtained for targets at even larger distances. Indeed, as explained in Section III, the differences between the propagation paths are smaller for targets at larger distances; therefore, the signal received by the different receivers is more similar to each other, better approximating the ideal case. This is also the reason why for targets at larger distance the optimum number of antennas is larger. However, for targets beyond around $D = 7$ cm, according to the approximated link budget, the final system S/N is calculated to be below the intended threshold (30 dB), because the improving factor is not able to compensate for the larger propagation losses.

Overall, it is worth observing that once the maximum target distance is calculated (for example, in this case, $D = 7$ cm), then the total number of antennas for the system is derived, possibly with a compromise for the lateral resolution, as already discussed. However, the imaging system would benefit from a shelllike design, where only a fraction of the antennas are actually routed to the correlator according to the intended distance of the portion of the breast to be imaged, thus maximizing the system S/N for any distance.

To minimize the difference between the propagation paths, a conformal (spherical to fit the requirements for breast cancer detection) system architecture can be used, as shown in Fig. 7. Indeed, it is observed that, for a given spherical radius, if the target is placed at the center of the sphere all the propagation paths are equal to each other, allowing a perfect improving factor to be achieved, regardless of the propagation losses. For targets placed with a displacement with respect to the center of the sphere, the conformal architecture still minimizes the differences, generating a better improving factor with respect to the nonconformal case.

The approach and the parameters for the calculation of the approximated link budget are the same as those used for the linear case, and the results are shown in Fig. 8. As an example, a spherical radius of 5 cm (representative of an average breast) is taken, and two different target distances are discussed, $D = 2$ cm and $D = 4$ cm. A number of results can be derived. First, also for the conformal architecture, an optimum exists. For $D = 2$ cm, this optimum is represented by a number of antennas $M_L = 5$; for $D = 4$ cm, this optimum is represented by a number of antennas $M_L = 13$. Second, the achieved improving factor, while still being smaller than what achievable in the ideal lossless case, is improved with respect to the nonconformal architecture, as expected. Indeed, for $D = 2$ cm and $M_L = 5$ (optimum), the improving factor is around 6.5, around 3.1 times lower than $M_L(M_L - 1) = 20$, while for $D = 4$ cm and $M_L = 13$ (optimum), the improving factor is around 43, around 3.6 times lower than $M_L(M_L - 1) = 156$. It is worth observing that, in Fig. 8, the curve for $D = 5$ cm (target at the center of the sphere) is not reported, because, as anticipated, it represents the ideal case where all propagation paths are identical and the ideal improving factor is achieved for any number of antennas.

Overall, the improvement given by the conformal architecture is clear, in terms of the higher improving factor (i.e., of the final system S/N) and in terms of available antennas, with an impact also on the resolution. In addition, also for the case of the conformal architecture, it is expected a shelllike design, where only a fraction of the antennas are actually routed to the correlator according to the intended distance of the portion of the breast to be imaged, thus maximizing the system S/N for any distance.

V. System Architecture—Validation

In order to validate the system design described in Section IV, a full-wave model (based on a commercial software using a frequency-domain solver) of the conformal architecture is implemented. In particular, a breast radius of 5 cm is used, with a target at $D = 4$ cm. Under these hypotheses, the optimum number of antennas is $M_L = 13$, which corresponds to a total number of antennas $M = 2M_L + 1 = 27$, as outlined in Section IV. However, as shown in Fig. 8, the number of radiators can be increased up to $M_L = 16$ (i.e., $M = 33$), improving the resolution, with limited deterioration of the improving factor. Therefore, a total number of antennas $M = 32$ is designed for this validation. As anticipated, the radiators are open-ended WR28 waveguides, with a fundamental-mode bandwidth from

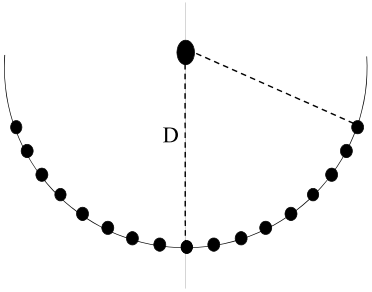

Fig. 7. Schema of the conformal architecture. The symmetry plane is depicted as the central light gray line.

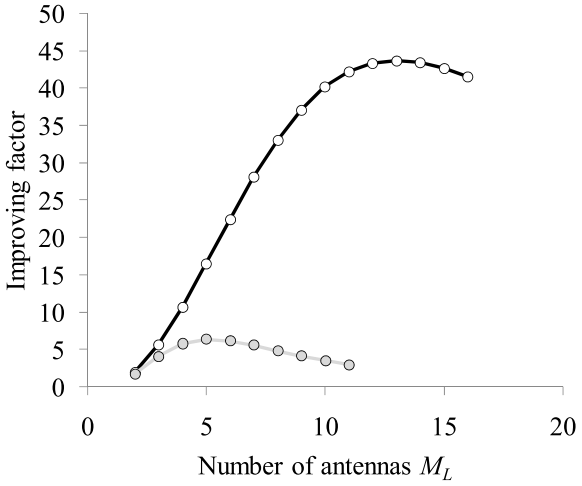

Fig. 8. Improving factor for a conformal architecture for a target distance $D = 2$ cm (light gray line) and $D = 4$ cm (black line).

26.5 to 40 GHz. Open-ended WR28 waveguides represent a convenient choice for the integration in the whole array, with a broad radiation pattern able to provide a coverage on the entire breast.

The target is modeled as a sphere with a diameter of 2 mm, in line with the expected system resolution. For the first test case a sphere made out of perfect metal is considered, while for the second test case the sphere is assumed to be made of tumorous tissue (*realistic case*). Both for the breast tissue and the tumorous tissue, the parameters reported in Table III are used. It is worth noting that, to reduce the computational effort, the full-wave model is simplified not including the skin. Indeed, the volume to be meshed for a breast radius of 5 cm is around $1360\lambda^3$, where λ is the wavelength in the breast tissue, calculated according to Table III. If a 2-mm-thick skin was included in the full-wave model, it would add a volume in the order of $2750\lambda^3$, tripling the total model dimension. Still, even neglecting in the full-wave model the extra losses given by the skin (but they are accounted for in the link budget study in Section IV when determining the optimum number of antennas), the full-wave model is representative of the intended scenario, which is mainly devised to validate the system architecture in terms of image formation at mm-waves within a dissipative medium, for a conformal layout.

To obtain the image, two different sets of scattering parameters are calculated. First, the scattering parameters with the target are calculated. Then, the scattering parameters without the target are calculated, and the latter are subtracted from

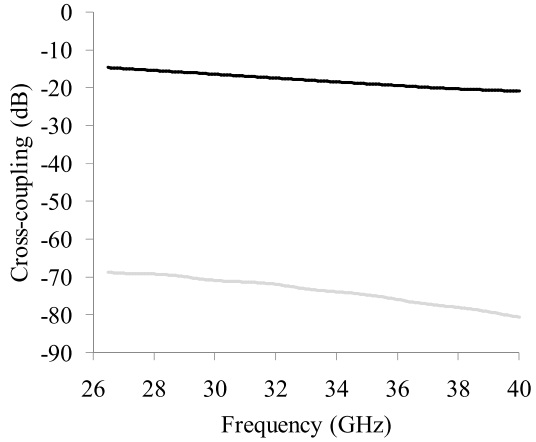

Fig. 9. Cross coupling between antennas 1 and 2 (black line) and between antennas 1 and 32 (gray line), as labeled in Figs. 10 and 11.

the former to calibrate out any spurious effect, including the crosstalk with adjacent antennas, which is shown in Fig. 9, for two notable combinations, namely between consecutive antennas (antennas 1 and 2 in Figs. 10 and 11) and between opposite antennas (antennas 1 and 32 in Figs. 10 and 11).

The final set of calibrated scattering parameters is then used as input for the image reconstruction technique, which is implemented in MathWorks MATLAB. In particular, a delay-multiply-and-sum (DMAS)-based beamforming algorithm, proposed also for ultrasound B-mode imaging and called Filtered-DMAS (F-DMAS), is used for image formation [39], [40]. To compute the RF signals received by each antenna, a Gaussian pulse ρ_{TX} with a standard deviation $\sigma = 50.6$ ps, a central frequency $f = 33.25$ GHz and a fractional bandwidth (measured at a taper of -20 dB) of around 40% (26.5–40 GHz), is synthetized.

This means practically that the entire spectrum associated with the pulse is compatible with the bandwidth of the open-ended WR28 antenna. In addition, the pulse peak is at $t_0 = 4\sigma$. Thus, the transmitted signal can be written as

$$\rho_{\mathrm{TX}} = \cos(2\pi f(t - t_0)) \cdot \exp(-(t - t_0)^2/\sigma^2). \tag{3}$$

Then, the transmitted signal is convolved with the scattering parameters provided by the full-wave solver. In this way, the signal received by each receiving antenna is calculated. This step is followed by synthetic focusing in each point of the image. The signals are realigned in the time domain (i.e., focused) by computing the transmit/receive delays for each antenna pair and each focal point in the considered image space (i.e., the two-way propagation time from the transmitting antenna to the focal point, and back to the receiving antenna). An amplitude equalization factor equal to the product of the transmission and reception path distances is also applied to each image point to compensate for the wave geometrical spreading. The signals are then beamformed by implementing the steps of the F-DMAS algorithm described in [40], which has already been tested also in synthetic-aperture ultrasound imaging [41], [42]. In this case actually, all the signals received after each transmit event (i.e., $32 \times 31 = 992$ signals) are considered as inputs of the beamformer, further enhancing target detection. With respect to other standard algorithms, F-DMAS provides improved performance in terms

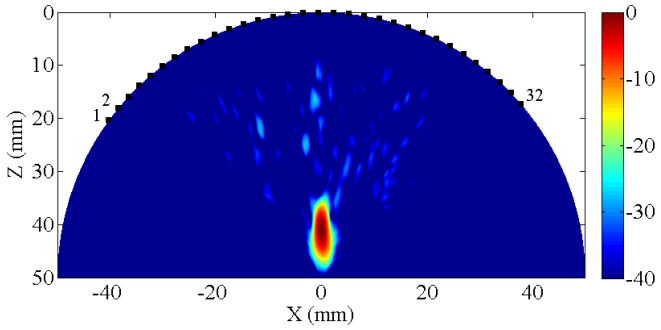

Fig. 10. Image obtained using the F-DMAS algorithm for a target (metal sphere, diameter 2 mm) at 40 mm from the conformal antenna plane (breast radius 50 mm), comprising 32 antennas working in the frequency range of 26.5–40 GHz. Color scale in decibel.

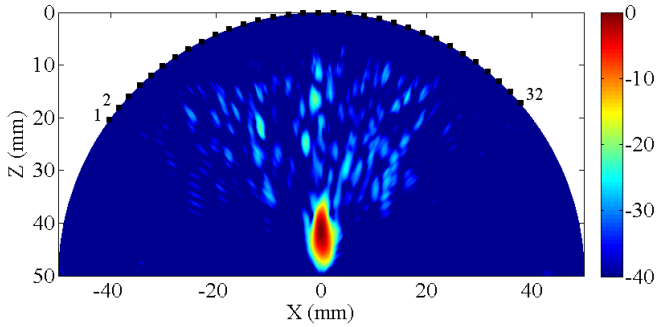

Fig. 11. Image obtained using the F-DMAS algorithm for a target (sphere made of tumorous tissue) at 40 mm from the conformal antenna plane (breast radius 50 mm), comprising 32 antennas working in the frequency range of 26.5–40 GHz. Color scale in decibel.

of both beam sidelobe reduction and main-lobe narrowing (i.e., a higher image lateral resolution and contrast). The final image is obtained after normal image formation techniques, including envelope detection, amplitude normalization, and logarithmic compression.

The results are shown in Figs. 10 and 11 for the metal sphere and the realistic case, respectively. It is shown that the target position, identified by the peak position, is at a depth of around 41 mm, with a lateral displacement of around 0.2 mm. This can be considered in good agreement with the theoretical depth of 40 mm. In addition, the measured range and lateral resolution (at -6 dB) are approximately $\delta_R = 7.0$ mm and $\delta_L = 2.2$ mm, respectively, for the metal target, and $\delta_R = 7.0$ mm and $\delta_L = 2.3$ mm, respectively, for the realistic target.

VI. Conclusion

This paper presented the possibility to use mm-waves to realize a breast imaging system. For the first time, the system layout and architecture are designed and optimized based on experimental data for the dielectric permittivity of the breast tissue and taking into account the safety aspects related to the body exposure to a relatively high level of electromagnetic power.

It is demonstrated, using multiphysics and full-wave models, that a penetration depth of several centimeters can be obtained, and that conformal system layouts are capable of delivering significantly better performance than linear layouts. For a relevant example (i.e., breast radius 50 mm, target depth 40 mm, conformal architecture with 32 antennas working in the frequency range 26.5–40 GHz), the breast image is reconstructed using an advanced image formation technique (F-DMAS), showing that the target can be clearly detected.

Acknowledgment

The authors thank C. Fodor, Department of Medical Imaging and Radiation Sciences, European Institute of Oncology, Milan, Italy, for her support in study coordination and data management. The authors are grateful to the gross pathology assistants and technicians in the Department of Pathology and Laboratory Medicine, European Institute of Oncology, Milan, for their assistance in preparing the tissue samples for this work.

References

[1] N. K. Nikolova, "Microwave imaging for breast cancer," *IEEE Microw. Mag.*, vol. 12, no. 7, pp. 78–94, Dec. 2011.

[2] M. Klemm, I. J. Craddock, J. A. Leendertz, A. Preece, and R. Benjamin, "Radar-based breast cancer detection using a hemispherical antenna array—Experimental results," *IEEE Trans. Antennas Propag.*, vol. 57, no. 6, pp. 1692–1704, Jun. 2009.

[3] T. M. Grzegorczyk, P. M. Meaney, P. A. Kaufman, R. M. DiFlorio-Alexander, and K. D. Paulsen, "Fast 3-D tomographic microwave imaging for breast cancer detection," *IEEE Trans. Med. Imag.*, vol. 31, no. 8, pp. 1584–1592, Aug. 2012.

[4] E. C. Fear, J. Bourqui, C. Curtis, D. Mew, B. Docktor, and C. Romano, "Microwave breast imaging with a monostatic radar-based system: A study of application to patients," *IEEE Trans. Microw. Theory Techn.*, vol. 61, no. 5, pp. 2119–2128, May 2013.

[5] M. J. Burfeindt, J. D. Shea, B. D. Van Veen, and S. C. Hagness, "Beamforming-enhanced inverse scattering for microwave breast imaging," *IEEE Trans. Antennas Propag.*, vol. 62, no. 10, pp. 5126–5132, Jun. 2009.

[6] H. Bahramiabarghouei, E. Porter, A. Santorelli, B. Gosselin, M. Popovic, and L. A. Rusch, "Flexible 16 antenna array for microwave breast cancer detection," *IEEE Trans. Biomed. Eng.*, vol. 62, no. 10, pp. 2516–2525, Oct. 2015.

[7] M. Lazebnik *et al.*, "A large-scale study of the ultrawideband microwave dielectric properties of normal breast tissue obtained from eduction surgeries," *Phys. Med. Biol.*, vol. 52, no. 10, pp. 2637–2656, 2007.

[8] M. Lazebnik *et al.*, "A large-scale study of the ultrawideband microwave dielectric properties of normal, benign and malignant breast tissues obtained from cancer surgeries," *Phys. Med. Biol.*, vol. 52, no. 20, pp. 6093–6115, 2007.

[9] M. Klemm, I. J. Craddock, and A. W. Preece, "Contrast-enhanced breast cancer detection using dynamic microwave imaging," in *Proc. IEEE Antennas Propag. Soc. Int. Symp.*, Chicago, IL, USA, Jul. 2012, pp. 1–2.

[10] F. Töpfer and J. Oberhammer, "Millimeter-wave tissue diagnosis: The most promising fields for medical applications," *IEEE Microw. Mag.*, vol. 16, no. 4, pp. 97–113, May 2015.

[11] A. Taeb, S. Gigoyan, and S. Safavi-Naeini, "Millimetre-wave waveguide reflectometers for early detection of skin cancer," *IET Microw., Antennas Propag.*, vol. 7, no. 14, pp. 1182–1186, Nov. 2013.

[12] A. Fitzgerald *et al.*, "Terahertz pulsed imaging of human breast tumors," *Radiology*, vol. 239, no. 2, pp. 533–540, May 2006.

[13] D. Bennett *et al.*, "Assessment of corneal hydration sensing in the terahertz band: *In vivo* results at 100 GHz," *J. Biomed. Opt.*, vol. 17, no. 9, p. 097008, Sep. 2012.

[14] Y. Nikawa, N. Hoshi, K. Kawai, and S. Ebisu, "Study on dental diagnosis and treatment using millimeter waves," *IEEE Trans. Microw. Theory Techn.*, vol. 48, no. 11, pp. 1783–1788, Nov. 2000.

[15] S. Moscato *et al.*, "A mm-Wave 2D ultra-wideband imaging radar for breast cancer detection," *Int. J. Antennas Propag.*, vol. 2013, 2013, Art. no. 475375, doi: 10.1155/2013/475375.

[16] M. Bassi, M. Caruso, M. S. Khan, A. Bevilacqua, A. Capobianco, and A. Neviani, "An integrated microwave imaging radar with planar antennas for breast cancer detection," *IEEE Trans. Microw. Theory Techn.*, vol. 61, no. 5, pp. 2108–2118, May 2013.

[17] L. Chao, M. Afsar, and K. Korolev, "Millimeter wave dielectric spectroscopy and breast cancer imaging," in *Proc. 7th Eur. Microw. Integr. Circuits Conf. (EuMIC)*, vol. 2. Amsterdam, The Netherlands, Oct. 2012, pp. 572–575.

[18] C. Yu, S. Fan, Y. Sun, and E. Pickwell-MacPherson, "The potential of terahertz imaging for cancer diagnosis: A review of investigations to date," *Quant. Imag. Med. Surgery*, vol. 2, no. 1, pp. 33–45, Mar. 2012.

[19] S. J. Erickson-Bhatt *et al.*, "Noninvasive surface imaging of breast cancer in humans using a hand-held optical imager," *Biomed. Phys. Eng. Exp.*, vol. 1, no. 4, pp. 045001-1–045001-11, 2015.

[20] W. J. Fleming, "Forty-year review of automotive electronics," *IEEE Veh. Technol. Mag.*, vol. 10, no. 3, pp. 80–90, Sep. 2015.

[21] S. S. Ahmed, A. Genghammer, A. Schiessl, and L.-P. Schmidt, "Fully electronic E-band personnel imager of 2 m ^{2} aperture based on a multistatic architecture," *IEEE Trans. Microw. Theory Techn.*, vol. 61, no. 1, pp. 651–657, Jan. 2013.

[22] J. Antes and I. Kallfass, "Performance estimation for broadband multi-gigabit millimeter- and sub-millimeter-wave wireless communication links," *IEEE Trans. Microw. Theory Techn.*, vol. 63, no. 10, pp. 3288–3299 Jan. 2013.

[23] A. Martellosio *et al.*, "0.5–50 GHz dielectric characterisation of breast cancer tissues," *Electron. Lett.*, vol. 51, no. 13, pp. 974–975, Jun. 2015.

[24] A. Martellosio *et al.*, "Dielectric properties characterization from 0.5 to 50 GHz of breast cancer tissues," *IEEE Trans. Microw. Theory Techn.*, to be published, doi: 10.1109/TMTT.2016.2631162.

[25] T. Wu, T. S. Rappaport, and C. M. Collins, "Safe for generations to come: Considerations of safety for millimeter waves in wireless communications," *IEEE Microw. Mag.*, vol. 16, no. 2, pp. 65–84, Mar. 2015.

[26] P. F. Espín-López *et al.*, "Breast cancer imaging at mm-Waves: Feasibility study on the safety exposure limits," in *Proc. 46th Eur. Microw. Conf. (EuMC)*, London, U.K., Oct. 2016, pp. 667–670.

[27] "Guidelines for limiting exposure to time-varying electric, magnetic, and electromagnetic fields (up to 300 GHz)," *Health Phys.*, vol. 74, no. 4, pp. 494–522, Apr. 1998.

[28] M. Zhadobov, N. Chahat, R. Sauleau, C. Le Quement, and Y. Le Drean, "Millimeter-wave interactions with the human body: State of knowledge and recent advances," *Int. J. Microw. Wireless Technol.*, vol. 3, no. 2, pp. 237–247, Apr. 2011.

[29] A. I. Sabbah, N. I. Dib, and M. A. Al-Nimr, "Evaluation of specific absorption rate and temperature elevation in a multi-layered human head model exposed to radio frequency radiation using the finite-difference time domain method," *IET Microw., Antennas Propag.*, vol. 5, no. 9, pp. 1073–1080, Jun. 2011.

[30] J. Accardo and M. A. Chaudhry, "Radiation exposure and privacy concerns surrounding full-body scanners in airports," *J. Radiat. Res. Appl. Sci.*, vol. 7, no. 2, pp. 198–200, 2014.

[31] E. Zastrow, S. K. Davis, and S. C. Hagness, "Safety assessment of breast cancer detection via ultrawideband microwave radar operating in pulsed-radiation mode," *Microw. Wireless Technol. Lett.*, vol. 49, no. 1, pp. 221–225, Jan. 2007.

[32] A. Santorelli, M. V. Schueren, and M. Popovic, "SAR levels in microwave breast imaging: 3-D safety assessment with plane-wave illumination," in *Proc. Asia–Pacific Microw. Conf.*, Melbourne, VIC, Australia, Dec. 2011, pp. 481–484.

[33] V. De Santis, J. Bourqui, and E. C. Fear, "Safety assessment of microwave breast imaging techniques: A comparison between two different approaches," in *Proc. 30th General Assembly Sci. Symp. (URSI)*, Istanbul, Turkey, Aug. 2011, pp. 1–4.

[34] C. Gabriel, S. Gabriel, and E. Corthout, "The dielectric properties of biological tissues: I. Literature survey," *Phys. Med. Biol.*, vol. 41, no. 11, pp. 2231–2249, Nov. 1996.

[35] P. S. Yarmolenko *et al.*, "Thresholds for thermal damage to normal tissue: An update," *Int. J. Hyperthermia*, vol. 27, no. 4, pp. 320–343, 2011.

[36] C.-H. Wang, Y.-T. Chiu, and Y.-S. Lin, "3.1 dB NF 20-29 GHz CMOS UWB LNA using a T-match input network," *Electron. Lett.*, vol. 46, no. 19, pp. 1312–1313, Sep. 2010.

[37] F. Vecchi *et al.*, "A wideband receiver for multi-Gbit/s communications in 65 nm CMOS," *IEEE J. Solid-State Circuits*, vol. 46, no. 3, pp. 551–561, Mar. 2011.

[38] K. Hadipour, A. Ghiglioni, A. Mazzanti, M. Bassi, and F. Svelto, "A 40GHz to 67GHz bandwidth 23dB gain 5.8dB maximum NF mm-wave LNA in 28nm CMOS," in *Proc. IEEE Radio Freq. Integr. Circuits Symp. (RFIC)*, Phoenix, AZ, USA, May 2015, pp. 327–330.

[39] H. B. Lim, N. T. Nhung, E. P. Li, and N. D. Thang, "Confocal microwave imaging for breast cancer detection: Delay-multiply-and-sum image reconstruction algorithm," *IEEE Trans. Biomed. Eng.*, vol. 55, no. 6, pp. 1697–1704, Jun. 2008.

[40] G. Matrone, A. S. Savoia, G. Caliano, and G. Magenes, "The delay multiply and sum beamforming algorithm in ultrasound B-mode medical imaging," *IEEE Trans. Med. Imag.*, vol. 34, no. 4, pp. 940–949, Apr. 2015.

[41] G. Matrone, A. S. Savoia, G. Caliano, and G. Magenes, "Ultrasound synthetic aperture focusing with the delay multiply and sum beamforming algorithm," in *Proc. IEEE Int. Conf. Eng. Med. Biol. Soc. (EMBC)*, Milan, Italy, Aug. 2015, pp. 137–140.

[42] G. Matrone, A. S. Savoia, G. Caliano, and G. Magenes, "Depth-of-field enhancement in filtered-delay multiply and sum beamformed images using synthetic aperture focusing," *Ultrasonics*, vol. 75, pp. 216–225, Mar. 2017.

Simona Di Meo (S'14) was born in Foggia, Italy, in 1992. She received the B.S. degree in electronics and computer science and M.S. degree *(cum laude)* in electronic engineering from the University of Pavia, Pavia, Italy, in 2014 and 2016, respectively, where she is currently pursuing the Ph.D. degree in electronics.

She is currently involved in the design of mm-wave imaging systems based on multistatic radar architectures. Her current research interests include innovative techniques for early breast cancer detection.

Ms. Di Meo was a recipient of a competitive grant from the IEEE Antennas and Propagation Society in 2015.

Pedro Fidel Espín-López (S'16) was born in Murcia, Spain, in 1989. He received the M.S. degree in electronic engineering from the Technical University of Cartagena, Murcia, in 2015. He is currently pursuing the Ph.D. degree in electronics at the University of Pavia, Pavia, Italy.

In 2015, he joined the European Institute of Oncology, Milan, Italy, as a Research Fellow. He was involved in the study of nonionizing dosimetry and the assessment of safety for a breast cancer detection system using millimeter and submillimeter waves. His current research interests include the study and development of microwave and millimeter wave antenna systems.

Andrea Martellosio (S'14) was born in Lodi, Italy, in 1988. He received the M.S. degree in electronic engineering from the University of Pavia, Pavia, Italy, in 2013, where he is currently pursuing the Ph.D. degree in electronics.

In 2014, he joined the European Institute of Oncology, Milan, Italy, as a Research Fellow, where he is focused on the 3-D imaging for breast cancer detection using millimeter and submillimeter waves. His current research interests include the study and development of microwave and millimeter wave antenna systems.

Marco Pasian (S'06–M'09–SM'15) was born in 1980. He received the M.Sc. degree *(cum laude)* in electronic engineering and Ph.D. degree in electronics and computer science from the University of Pavia, Pavia, Italy, in 2005 and 2009, respectively.

He held a post-doctoral position with the University of Pavia, from 2009 to 2013. He joined the European Space Agency, Darmstadt, Germany, in 2004; Carlo Gavazzi Space, Milan, Italy, in 2005; and the TNO, Defense, Security and Safety, The Netherlands, in 2008. Since 2013, he has been a Research Fellow with the Microwave Laboratory, University of Pavia.

Dr. Pasian is a member of the European Microwave Association (EuMA). He was a recipient of a competitive grant from the Italian Ministry of Education, University, and Research under the funding schema Scientific Independence of Young Researchers. He was the Technical Program Co-Chair at the European Microwave Conference 2014, the Conference Prize Committee Chair at European Microwave Week 2014, and the Finance Chair at the IEEE International Conference on Numerical and Electromagnetic Modeling and Optimization. He is an Associate Editor of the EuMA *International Journal of Microwave and Wireless Technologies.*

Giulia Matrone (M'09) was born in Pavia, Italy, in 1985. She received the B.Sc. and M.Sc. degrees *(cum laude)* in biomedical engineering and Ph.D. degree in bioengineering and bioinformatics from the University of Pavia, Pavia, in 2006, 2008, and 2012, respectively.

From 2012 to 2016, she was a Post-Doctoral Researcher with the Bioengineering Laboratory, Department of Electrical, Computer and Biomedical Engineering, University of Pavia, where she is currently an Assistant Professor. Her current research interests are mainly in the field of ultrasound medical imaging and signal processing; they include beam-forming and imaging techniques, simulations, system-level analyses for the design of 3-D ultrasound imaging probes, and microwave imaging for biomedical applications.

Maurizio Bozzi (S'98–M'01–SM'12) was born in Voghera, Italy, in 1971. He received the Ph.D. degree in electronics and computer science from the University of Pavia, Pavia, Italy, in 2000.

He held research positions with various universities worldwide, including the Technische Universität Darmstadt, Germany; Universitat de Valencia, Valencia, Spain; and École Polytechnique de Montréal, Montreal, QC, Canada. In 2002, he joined the Department of Electronics, University of Pavia. He was also a Guest Professor with the Tianjin University, Tianjin, China, from 2015 to 2017. He is currently an Associate Professor with the University of Pavia. He has authored or co-authored over 95 journal papers and 250 conference papers. He co-edited *Periodic Structures* (Res. Signpost, 2006) and co-authored *Microstrip Lines and Slotlines* (Artech House, 2013). His current research interests include the computational electromagnetics, substrate integrated waveguide technology, and use of novel materials and fabrication technologies for microwave circuits, including paper, textile, and 3-D printing.

Prof. Bozzi was a member of the General Assembly of the European Microwave Association from 2014 to 2016. He is currently an elected member of the Administrative Committee of the IEEE Microwave Theory and Techniques Society (MTT-S) from 2017 to 2019 and the Co-Chair of the Meeting and Symposia Committee of MTT-S AdCom in 2017. He was a recipient of several awards, including the 2015 Premium Award for Best Paper in *IET Microwaves, Antennas and Propagation*, the 2014 Premium Award for the Best Paper in *Electronics Letters*, the Best Student Paper Award at the 2016 IEEE Topical Conference on Wireless Sensors and Sensor Networks, the Best Paper Award at the 15th Mediterranean Microwave Symposium, the Best Student Award at the 4th European Conference on Antennas and Propagation, the Best Young Scientist Paper Award of the XXVII General Assembly of URSI in 2002, and the MECSA Prize of the Italian Conference on Electromagnetics, in 2000. He was the Secretary of the IEEE MTT-S in 2016. He is the General Chair of the IEEE MTT-S International Microwave Workshop Series–Advanced Materials and Processes, Pavia, in 2017. He was the General Chair at the IEEE International Conference on Numerical Electromagnetic Modeling and Optimization, Pavia, 2014, and the General Chair of the IEEE MTT-S International Microwave Workshop Series on Millimeter Wave Integration Technologies, Sitges, Spain, 2011. He is an Associate Editor of IEEE MICROWAVE AND WIRELESS COMPONENTS LETTERS, *IET Electronics Letters*, and *IET Microwaves, Antennas and Propagation*.

Giovanni Magenes (M'90) was born in Genoa, Italy, in 1956. He received the M.S. degree *(cum laude)* in electrical engineering from the University of Pavia, Pavia, Italy, in 1981, and the Ph.D. degree in biomedical engineering from the Politecnico di Milano, Milan, Italy, in 1987.

He was a Visiting Researcher with the Institut Nationale de la Sante et Réchérche Medicale, Lyon, France, and a Visiting Professor with the Faculté des Sciences, Université de la Mediterrane, Luminy, France. He was a leader of various international and national research projects in the field of biomedical engineering. He was the Director of the Department of Computer Engineering and Systems Science, University of Pavia, until 2012, where he is currently a Full Professor of biomedical signal and image processing. He is also with the Technological Innovation Section, European Centre for Training and Research in Earthquake Engineering, Pavia. His current research interests include signal and image processing in biomedical applications, soft computing methods, biomimetic sensors and devices, artificial sensorimotor systems, hybrid tissues, and wearable devices.

Andrea Mazzanti (S'02–M'09–SM'13) received the Laurea and Ph.D. degrees in electrical engineering from the Università di Modena and Reggio Emilia, Modena, Italy, in 2001 and 2005, respectively.

In 2003, he was with Agere Systems, Allentown, PA, USA, as an Intern. From 2006 to 2009, he was an Assistant Professor with the Università di Modena and Reggio Emilia. In 2010, he joined the University of Pavia, Pavia, Italy, where he is currently an Associate Professor. He has authored over 90 technical papers. His current research interests include device modeling and IC design for high-speed communications, RF, and millimeter-wave systems.

Dr. Mazzanti was a member of the Technical Program Committee of the IEEE Custom Integrated Circuit Conference (CICC) from 2008 to 2014 and has been a member of the IEEE European Solid State Circuits Conference (ESSCIRC) and the IEEE International Solid State Circuits Conference since 2014. He was an Associate Editor for the IEEE TRANSACTIONS ON CIRCUITS AND SYSTEMS—I: REGULAR PAPERS from 2012 to 2015 and a Guest Editor for special issues of the IEEE JOURNAL OF SOLID-STATE CIRCUITS dedicated to CICC from 2013 to 2014 and ESSCIRC in 2015.

Luca Perregrini (M'97–SM'12–F'16) was born in Sondrio, Italy, in 1964. He received the Laurea degree in electronic engineering and Ph.D. degree in electronics and computer science in 1989 and 1993, respectively.

In 1992, he joined the Faculty of Engineering, University of Pavia, Pavia, Italy. He was a Visiting Professor with the École Polytechnique de Montréal, Montreal, QC, Canada, in 2001, 2002, 2005, and 2006, respectively. He has been responsible for many research contracts with prominent international research centers and companies. He is currently a Full Professor of electromagnetic fields with the University of Pavia, where he is also responsible for the Microwave Laboratory. He has authored or co-authored over 86 journal papers and over 245 conference papers, 6 book chapters, 2 textbooks; and co-edited *Periodic Structures* (Res. Signpost, 2006). His current research interests include the development of numerical methods for electromagnetics, the design of microwave components and antennas, the development of numerical methods for electromagnetics, and the design of microwave components and antennas.

Prof. Perregrini served as a member of prize committees for several conferences/societies. He has been an invited speaker at many conferences and has delivered invited seminar talks in universities and research centers worldwide. He was a member of the General Assembly of the European Microwave Association (EuMA) from 2011 to 2013. He is a member of the Technical Committee Microwave Field Theory-15, the IEEE Microwave Theory and Technique Society (MTT-S), and the Board of Directors of EuMA. He was a co-recipient of several Best Paper Awards at international conferences. He was the appointed Technical Program Committee Chair of the International Microwave Workshop Series on Advanced Materials and Processes, Pavia, in 2017. He was the Technical Program Committee Chair of the IEEE MTT-S International Conference on Numerical Electromagnetic Modeling and Optimization, Pavia, in 2014, and of the European Microwave Conference, Rome, Italy, in 2014. He was an Associate Editor of IEEE MICROWAVE AND WIRELESS COMPONENTS LETTERS from 2010 to 2013, the IEEE TRANSACTIONS ON MICROWAVE THEORY AND TECHNIQUES from 2013 to 2016, the *International Journal of Microwave and Wireless Technologies* from 2011 to 2016, and the *IET Electronic Letters* from 2015 to 2016. He was a Guest Editor of the IEEE TRANSACTIONS ON MICROWAVE THEORY AND TECHNIQUES in 2015 and the *International Journal of Microwave and Wireless Technologies* in 2015. He is currently an Editor-in-Chief of the IEEE TRANSACTIONS ON MICROWAVE THEORY AND TECHNIQUE.

Francesco Svelto (S'93–M'98–SM'11–F'13) received the Laurea and Ph.D. degrees in electrical engineering from the University of Pavia, Pavia, Italy, in 1991 and 1995, respectively.

From 1995 to 1997, he held an industry grant for research in RF CMOS. In 1997, he joined the Università di Bergamo, Bergamo, Italy, as an Assistant Professor, and in 2000, he joined the University of Pavia. He has been a Technical Advisor of RFDomus Inc., a start-up company, which he co-founded in 2002 and dedicated to highly integrated GPS receivers. Since 2006, he has been the Director of the Scientific Laboratory, joint between Università di Pavia and STMicrolectronics, dedicated to research in microelectronics, with an emphasis on mm-wave systems for wireless communications, high-speed serial links, and ultrasound electronics for medical diagnostic. He is currently a Professor and a Vice-Rector for knowledge transfer with the University of Pavia.

Dr. Svelto has been a member of the Technical Program Committee of the International Solid State Circuits Conference, the Custom Integrated Circuits Conference, and the Bipolar/BiCMOS Circuits Technology Meeting. He was a co-recipient of the IEEE JOURNAL OF SOLID-STATE CIRCUITS 2003 Best Paper Award. He is currently a member of the Technical Program Committee at the IEEE European Solid State Circuits Conference. He is a Solid State Circuits Society Distinguished Lecturer. He served as an Associate Editor and a Guest Editor for a special issue of the IEEE JOURNAL OF SOLID-STATE CIRCUITS from 2003 to 2007, and in 2003, respectively.

Paul Eugene Summers received the B.S. degrees in physics and mathematics from the University of Alberta, Edmonton, AB, Canada, in 1987 and 1989, respectively, and the Ph.D. degree from King's College, University of London, London, U.K., in 1999.

He is currently a Researcher with the European Institute of Oncology, Milan, Italy, and the Fondazione IRCSS Ca Granda Ospedale Maggiore Policlinico, Milan. His current research interests include the application of magnetic resonance imaging in oncology, neuroradiology and neuroscience, and the medical applications of millimeter waves.

Dr. Summers is a member of ISMRM, ESMRMB, AIFM, and IPEM.

Giuseppe Renne was born in Cosenza, Italy, in 1957. He received the bachelor's degree from the Medical School, State University of Naples (II° Faculty) in 1981, the master's degree from the Department of Pathology, Niguarda Cà Granda Hospital, Milan, Italy, and from the UCSC-Policlinico A. Gemelli of Rome, Rome, Italy, and the Specialization degree in anatomic pathology from the Cattolica University Sacro Cuore of Rome, Rome.

He joined the Service of Surgical Pathology, Regional Hospital, Magenta, Italy, as a Deputy Director, in 1995, and the Service of Surgical Pathology, S. Carlo B. Hospital, Milan, as a Deputy Director in 1998. Since 1999, he has been a Deputy Director and since 2002, he has been a Senior Deputy Director with the Department of Pathology and the Laboratory Medicine, European Institute of Oncology (IEO), Milan. Since 2007, he has been the Co-Director of the Department of Pathology, IEO. Since 2015, he has been the Director of Uropathology and Intraoperative Diagnostic Unit, IEO. He has co-authored over 80 publications in peer-reviewed journals.

Lorenzo Preda was born in Pavia, Italy, in 1964. He received the bachelor's degree in medicine and surgery in 1989 and the master's degree in radiology from the University of Pavia, Pavia.

He was an Assistant with the Institute of Radiology, IRCCS Policlinico San Matteo, Pavia, from 1991 to 2001. He was an Adjunct Professor with the Postgraduate School of the Specialization in Radiology, Medicine and Surgery Faculty, University of Pavia, from 1996 to 1997 and from 2015 to 2016. Since 2006, he has been a Senior Deputy Director with the Division of Radiology, European Institute of Oncology, Milan, Italy. Since 2016, he has been an Associate Professor with the Department of Clinical-Surgical, Diagnostic and Pediatric Sciences, University of Pavia, and the Director of the Radiology Unit, National Center of Oncological Hadrontherapy (CNAO Foundation), Pavia. He has authored or co-authored about 90 papers.

Prof. Preda was a member of the Scientific Editorial Board of European Radiology from 2008 to 2014. He has been a Board Member of the Odontostomatological and Head-Neck Radiology Section, SIRM, since 2012, and a Board Member of the Italian Association of Cervico-Cephalic Oncology since 2015. He was a recipient of the Fellowship of the European Society of Head and Neck Radiology in 2013.

Massimo Bellomi received the bachelor's degree in medicine and surgery from the University of Milan, Milan, Italy, in 1975, the Specialization degree in hepatology in 1976, and the master's diploma in radiology and radiotherapy in 1980.

He was part of the team that introduced percutaneous biliary drainage and gastrointestinal interventional radiology in Italy and developed a number of techniques for interventional and diagnostic radiology. He also designed software for archiving radiologic examinations and for image processing and analysis. In 1984, 1988, and 1991, he was the Director of Operative Units and Research Projects in Oncology of the National Research Council. In 1994, he joined the Department of Radiology, European Institute of Oncology, Milan, as the Director. In 1998, he joined the Department of Health Sciences, University of Milan, as an Associate Professor of radiology. From 2000 to 2003, he was a member of the Ministry of Health Commission for studies in diagnostic imaging. From 2000 to 2003 and from 2009 to 2012, he was the Director of the Postgraduated School of Radiology, School of Medicine, University of Milan, where he was the President of the School in Imaging and Radiotherapy Techniques in 2012. He is currently a Principal Investigator in a numbers of clinical trials. He has authored 238 scientific publications, 23 of which are book chapters. He is an Editor of the *European Journal of Radiology* and *Cancer Imaging Journal.*

Prof. Bellomi is a member of several scientific societies, including the SIRM Italian Society of Radiology, the ICIS International Cancer Imaging Society, and the ESR European Society of Radiology. He was a founding member and the President of the ICIS International Cancer Imaging Society in 2003–2004. He was the recipient of several research grants for studies on liver and gastrointestinal pathologies at the University Hospital of Pennsylvania, Philadelphia, PA, USA, in 1980; the Thomas Jefferson University of Philadelphia, Philadelphia, in 1980; and the University of Lund, Lund, Sweden, in 1983.